Article

A Numerical Framework of Simulating Flow-Induced Deformation during Liquid Composite Moulding

Hatim Alotaibi [1,*], Constantinos Soutis [2,3], Dianyun Zhang [4] and Masoud Jabbari [5,*]

1 Institute of Earth and Space Science, King Abdulaziz City for Science and Technology, Riyadh 12354, Saudi Arabia
2 Department of Materials, The University of Manchester, Manchester M13 9PL, UK
3 Northwest Composites Centre, University of Manchester, Manchester M13 9PL, UK
4 School of Aeronautics and Astronautics, Purdue University, West Lafayette, IN 47907, USA
5 School of Mechanical Engineering, University of Leeds, Leeds LS2 9JT, UK
* Correspondence: htalotaibi@kacst.gov.sa (H.A.); m.jabbari@leeds.ac.uk (M.J.)

Abstract: Fibre deformation (or shearing of yarns) can develop during the liquid moulding of composites due to injection pressures or polymerisation (cross-linking) reactions (e.g., chemical shrinkage). On that premise, this may also induce potential residual stress–strain, warpage, and design defects in the composite part. In this paper, a developed numerical framework is customised to analyse deformations and the residual stress–strain of fibre (at a micro-scale) and yarns (at a meso-scale) during a liquid composite moulding (LCM) process cycle (fill and cure stages). This is achieved by linking flow simulations (coupled filling–curing simulation) to a transient structural model using ANSYS software. This work develops advanced User-Defined Functions (UDFs) and User-Defined Scalers (UDSs) to enhance the commercial CFD code with extra models for chemorheology, cure kinetics, heat generation, and permeability. Such models will be hooked within the conservation equations in the thermo-chemo-flow model and hence reflected by the structural model. In doing so, the knowledge of permeability, polymerisation, rheology, and mechanical response can be digitally obtained for more coherent and optimised manufacturing processes of advanced composites.

Keywords: composites manufacturing; multi-scale numerical modelling; chemo-rheology; mechanical response; deformation

1. Introduction

1.1. Background

Composite products—fibre-reinforced polymer (FRP) structures— have been, and are still, a potential for aerospace, automotive, marine, and energy sectors due to high strength–weight ratio, light weight, durability, design flexibility, and chemical resistance [1–5]. Composite materials have been shown to be an effective (lighter and stronger) substitute for metal alloys (conventional materials) over the last few decades. The ongoing (promising) research on the recycling (reuse) of FRP composites is, moreover, bringing attention and fostering the development of more advanced and rigorous numerical models—the control and optimisation of advanced composites fabrication. Not to mention, composites make a vital contribution to biomedical applications (e.g., piezoelectric micro-electromechanical system (piezoMEMS)—polymer-based biosensors) [6]. Such composites are usually made of two or more materials, e.g., a polymer matrix reinforced with fibres. Those polymers are classified into two types: thermoplastics and thermosets. Thermosetting polymers (e.g., epoxy, polyester, phenolic, and vinyl ester) retain a low viscosity (pre-polymerisation—liquid state) evoking better fibre impregnation (during mould filling) and superior mechanical integrity of the manufactured (polymerised—a glassy/solid state) composite parts [2–5]. On the other hand, thermoplastics—polyetherimide, polyether, polyphenylene sulfide, etc.—yield higher viscous liquids (at molten state), evoking impregnation difficulties when

reinforced with fibres and hence lower mechanical and physical characteristics of the final product [3,5,7,8]. On that premise, this present study is bounded to thermosets as a polymer type and puts emphasis on its impregnation (saturation of fibres) parameters, chemo-rheological behaviour, cure kinetics, flow-induced fibre deformation, and residual (internal) stress/strain.

Fibre-reinforced polymer composites are processed and fabricated using closed or open mould techniques. The open moulding would include hand lay-up, spray-up, and filament winding, while the closed moulding incorporates a wide range of processes like the well-known resin transfer moulding (RTM), autoclave, pultrusion, etc. [3–5]. The latter are commonly used by composite industries since they offer large-scale production, large/small, and complex-shaped parts. For this reason, the present research focuses more attention on the closed mould processes, in particular liquid composite moulding (LCM). Furthermore, fibre preforms/fabrics come in various classifications by which the broadly adopted ones in the liquid moulding of composites are mats, unidirectional (UD), weaves, braids, and knits [9]. A dual-scale fibrous porous medium falls under UD, weaves, and braids categories in which micro–meso-flow (two-scale) can take place.

Design and operation parameters dominate manufacturing phases (i.e., injection and cure) as well as contribute to the performance of the final product. Those would include ports/vents location and size, mould dimensions, pressure, temperature, and fibre preform permeability. Numerical methods can describe the multi-paradigm of physics using partial differential equations (PDEs) of a set of governing equations (e.g., Navier–Stokes (NS) for flow) on a discretised computational domain—a domain divided into grids or meshes. A diverse range of novel methods have been developed over the last decades including finite element method (FEM), finite volume method (FVM), and finite difference method (FDM. Some are superior to others; for example, FDM cannot be performed on a complex mesh (unstructured domain), while this can be quantified by FVM and FEM. This is unlike structural analysis by which the mechanics of materials, elasticity theory, and finite element are merely the mathematical approaches. The latter (FE), again, solves differential equations of mechanics and is more appropriate for structures of any size and complexity.

1.2. Summary of Previous Work

State-of-the-art reviews on mechanical response to resin flow and cure are briefly discussed within this section. A numerical analysis by Goncalves et al. [10] investigated micro-stresses during the composites (i.e., carbon/epoxy) manufacturing process—curing stage. The authors [10] used Abaqus (Finite Element Analysis Software) coupled with a thermo-curing model using the so-called user-subroutines—a customisation feature by Abaqus to enhance the commercial code for specific problems. The developed model was capable of capturing micro-stresses during the curing process and concluded that higher micro-mechanisms are found to be at thinner fibre/filament gaps due to chemical shrinkage or thermal expansion. Yuan et al. [11] developed a multi-scale model to characterise the influence of macro-stresses in composites on the micro-stresses during an autoclave curing process. Again, the authors [11] employed Abaqus coupled with UMATHT and USEFLD (user-subroutines) to link a thermo-chemical model for cure kinetics calculations. The work argued that temperature variations could affect the cross-linking polymer resin together with the fibre–resin interface, impacting the micro-mechanical properties. The influence of porosity of the fibrous porous medium on the residual stresses was studied by Dewangan et al. [12]. The paper used Abaqus-Fortran for mechanical and thermo-chemical modelling. The findings by the work [12] showed that the decrease in porosity will promote higher residual stresses. Peng et al. [13] characterised, using Abaqus, the influence of a thermosetting polymer cross-linking reaction (curing) on composite deformation at a macro-scale. The study [13] includes different stacking sequences (lay-ups) for each simulation, whereby lay-ups with 0/90 showed less deformation phenomena in comparison with 0/90 associated with 45/−45. A study by Kim et al. [14] focused on the woven-fabric-based L-shaped part and how such complex fabric architectures interact with liquid resin trans-

formation during cure—monomer to polymer. The authors [14] claimed that aside from the thermal expansion effect, the wider gaps between adjacent yarns feasibly provoked fibre deformations. A deep learning (convolutional neural network (CNN))-based work was elaborated by Fan et al. [15] to characterise the curing process-induced deformation of composite structures. The authors [15] used FE-based modelling to map various deformation scenarios of composites for different stacking sequences. A set of data collection was acquired for the CNN model and trained to obtain a map of process-induced deformations for a diversity of geometric shapes. The study [15] stressed the potential of the CNN model for capturing such complex mechanics in about ∼9 s compared with ∼6 min by the FE model.

1.3. Significance of the Present Work

The lack of research in reference to numerical prediction models of flow-induced residual stresses or strains in woven fabrics during the mould-filling process is evident. Furthermore, the shearing (or deformation) of yarns (fibre bundles) during such manufacturing processes is also an area of interest. The present work provides an all-inclusive numerical platform to waive the confined knowledge of complex flow mechanisms, including resin cure reaction, yarn deformation, and yarn residual stresses and strains, that take place during manufacturing processes of composites at the micro–meso-level—which is normally difficult to visualise by traditional methods.

2. Numerical Simulation Approach

The first aim of the present research is to develop a flow model that is capable of computing permeability, rheology, cure kinetics, and heat-transfer parameters of thermoset polymer resins in moulding processes of fibre preforms. The second aim of the research project is to design a numerical one-way fluid–structure interaction (FSI) framework—linking CFD to FEA—for solving residual stresses/strains and deformations of fibre bundles during liquid moulding and curing. This brings a simultaneous data linkage between fluids (thermoset resins) and structures (fibres), i.e., an all-inclusive thermo-chemo-visco-elastic modelling. Wherefore, the objectives—actions to achieve the aforementioned aims—are to create User-Defined Functions (UDFs), User-Defined Scalers (UDSs), and User-Defined Memories (UDMs) using C-based programming language for heat generation (used in energy equation), polymerisation (used in species transport equation), and micro-flow (used in Navier–Stokes equation) terms. Following this, the created codes are integrated into ANSYS Fluent solver to access conservation equations (via source terms) and perform the required tasks. The numerical simulations are to be performed on a representative unit cell (RUC) of a woven fabric that is designed by ANSYS DesignModeler—a parametric CAD (Computer-Aided Design) modeler.

To summarise, the aims of this research are to develop a rigorous numerical framework as a means to control and optimise manufacturing processes for advanced composites:

I. Develop a computational thermo-chemo-flow model that is capable of calculating the permeability, rheology, cure kinetics, and heat-transfer parameters of thermoset resins during the moulding of fibre preforms.

II. Design a numerical one-way fluid–structure interaction (FSI) framework—linking CFD to FEA—to solve residual stresses/strains, and deformations of fibre bundles during fill and cure process cycles.

The research framework and phase linkage are best described by Figure 1.
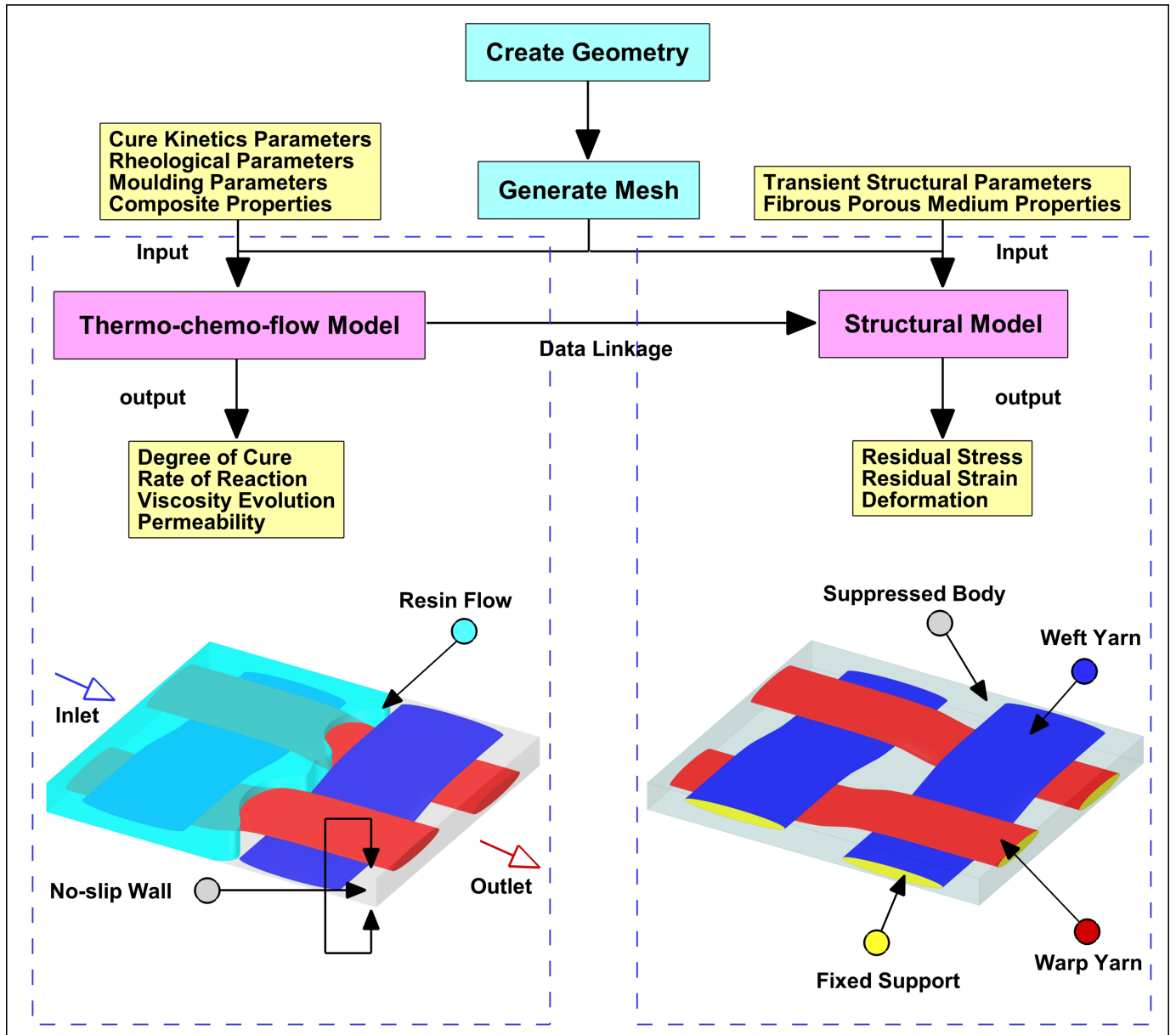
Figure 1. The framework of numerical one-way fluid–structure interaction (FSI)—linking CFD to FEA.

2.1. Thermo-Chemo-Flow Model

2.1.1. Flow Model

Flow is solved using Navier–Stokes (N–S) equations (incompressible viscous flows) together with the continuity equation as given below in Equations (1) and (2)

$$\frac{\partial}{\partial t}(\rho \mathbf{u}) + \nabla \cdot (\rho \mathbf{u}\mathbf{u}) = -\nabla p + \mu \nabla^2 \mathbf{u} + \rho \mathbf{g} + S \qquad (1)$$

$$\frac{\partial \rho}{\partial t} + \nabla \cdot (\rho \mathbf{u}) = 0 \qquad (2)$$

where $\mathbf{u}$ is the volume-averaged velocity, ∇p is the pressure gradient, $\rho \mathbf{g}$ is the body force term, $\mu \nabla^2 \mathbf{u}$ is the diffusion term, and the left-hand side of Equation (1) is the inertial forces term. It is worth noting that the volume-averaged velocity ($\mathbf{u}$)—or the so-called Darcy-averaged velocity—is defined as (equated to) flow-front velocity associated with medium porosity such that $\mathbf{u} = \mathbf{u}_{\text{ff}}\phi$ during the liquid moulding (filling) process [16]. Since slow flow

regimes (creeping/viscous flows) are seen in an LCM process (e.g., VARTM), this brings about a low Reynold number ($R_e \ll 1$) by which the viscous forces dominate the inertial forces. This reduces (N–S) to the so-called Stokes flow equation by eliminating the inertial term along with no external body forces acting on the flow. The Stokes equation particularly solves flows in the open region (inter-tow); for this reason, this necessitates adding a source term to account for flows within the porous region (intra-tow), leading to the well-known Stokes–Brinkman relationship—see Equation (3) (transient-sate form) [16–20].

$$\frac{\partial}{\partial t}(\rho \mathbf{u}) = -\nabla p + \mu \nabla^2 \mathbf{u} + S \tag{3}$$

$$\nabla \cdot \mathbf{u} = 0 \tag{4}$$

$$S = -\frac{\mu}{\mathbf{K}_t}\mathbf{u} \tag{5}$$

The $\mathbf{K}_t$ is the tensorial form of the micro-permeability—parallel ($K_{t\parallel}$) and perpendicular ($K_{t\perp}$) to fibres (filaments). Such a flow parameter can be calculated using the available theoretical/analytical models from the literature [21–27]. Here, Gebart [25] models are employed for parallel (longitudinal) and perpendicular (transverse) microscopic permeabilities—see Equations (6) and (7) (assuming hexagonal packing arrangement).

$$K_{t\parallel} = \frac{8r^2}{c}\frac{\left(1-V_f\right)^3}{V_f^2} \tag{6}$$

$$K_{t\perp} = r^2 * C_1 \left(\sqrt{\frac{V_{f\,\text{max}}}{V_f}} - 1\right)^{\frac{5}{2}} \tag{7}$$

$$\text{Hexagonal} \Rightarrow C_1 = \frac{16}{9\pi\sqrt{6}}, V_{f\,\text{max}} = \frac{\pi}{2\sqrt{3}}, c = 53 \tag{8}$$

In general, the computed volume-averaged velocity ($\mathbf{u}$) from Equations (3) and (4) that considered micro–meso regions—intra- and inter-tow—is used in the generalised form of Darcy's law (see Equations (9) and (10)) to calculate the dual-scale or the so-called global permeability.

$$\mathbf{u} = -\frac{\mathbf{K}_o}{\mu}\nabla p \tag{9}$$

where $\mathbf{K}_o$ is the global permeability tensor, μ is the viscosity, and ∇p is the pressure gradient. Assuming a homogenous porous medium with an orthotropic permeability—neglecting all off-diagonal components K_{ij}—Equation (9) becomes the following [28]:

$$\begin{bmatrix} u_x \\ u_y \\ u_z \end{bmatrix} = -\frac{1}{\mu}\begin{bmatrix} K_{xx} & 0 & 0 \\ 0 & K_{yy} & 0 \\ 0 & 0 & K_{zz} \end{bmatrix} \times \begin{bmatrix} \partial p/\partial p \\ \partial p/\partial y \\ \partial p/\partial z \end{bmatrix} \tag{10}$$

where K_{xx} and K_{yy} are in-plane permeabilities and K_{zz} is the through-thickness (transverse) permeability. In the event that a resin viscosity is not assumed constant during the mould filling due to stimulated potential cross-linking reactions by heat (mould-wall temperature) or a catalyst. The present numerical framework employs a Castro Macosko model [29] (i.e., a chemo-rheological model) by creating a UDF-UDS to integrate time–temperature–cure-dependent viscosity (see Equation (11)) into the conservation equations during filling and post-filling stages.

$$\mu(\alpha, T) = \mu_0 \exp\left(\frac{E_\mu}{RT}\right)\left(\frac{\alpha_{gel}}{\alpha_{gel} - \alpha}\right)^{a+b\alpha} \tag{11}$$

where α is the degree of cure, α_{gel} is the degree of cure at a gelation point, and E_μ, T, and R represent the viscosity activation energy, temperature, and gas constant, respectively. μ_0, a, and b are referred to as a pre-exponential factor and exponents.

2.1.2. Heat Transfer and Cure Model

Generally, the momentum and continuity equations are sufficient to solve a flow problem (resin infusion) on the assumption that no chemical reactions (polymerisation) or change in viscosity take place during the mould-filling stage. Such an assumption vanishes in case of heat (e.g., mould-wall temperature) or nanomaterial (e.g., graphene) involvement during the fabrication process (filling and post-filling stages). In such a manner, the flow becomes a convection–diffusion–reaction-dominated transport problem which requires coupling the energy and species equations with the flow equations during impregnation process. Once a complete filling is achieved, the post-filling phase is being solved by the energy and species equations until the cure is finished. Considering slow flow conditions, which is common in RTM/VARTM, provokes a small (approaching zero) Péclet number—Graetz number ($Gz \ll 1$)—(owing to small velocity, e.g., 0.001–1×10^{-5} [m/s]); hence, that manifests the assumption of local thermal equilibrium along with no contribution of thermal dispersion and viscous dissipation to the energy equation [30–35]. Thus, the energy equation can be expressed as follows:

$$\rho C_P \frac{\partial T}{\partial t} + \rho_r C_{P_r}(\mathbf{u} \cdot \nabla T) = \nabla(\mathbf{K}_T \cdot \nabla T) + \phi \rho_r \Delta H \dot{\alpha}(\alpha, T, t) \tag{12}$$

$$\begin{cases} \rho = \frac{(\rho_f \rho_r)}{(\rho_f w_r + \rho_r w_f)} \\ K_{T_\parallel} = w_r k_r + w_f k_f, \ K_{T_\perp} = \frac{(k_f k_r)}{(k_f w_r + k_r w_f)} \\ C_P = w_r C_{P_r} + w_f C_{P_f} \\ w_r = \frac{(\phi / \rho_f)}{\left(\frac{\phi}{\rho_f} + \frac{1 - \phi}{\rho_r}\right)} \\ w_f = 1 - w_r \end{cases} \tag{13}$$

where ρ [kg/m^3], C_p [J/kg$\cdot$K], $\mathbf{K}_T$ [W/m$\cdot$K], ϕ [$-$], and w [$-$] are the density, specific heat, thermal conductivity, porosity, and weight fraction, respectively. The fibre and resin subscripts are defined by f and r, respectively. ΔH [J/g] is the total heat of the reaction, and $\dot{\alpha}(\alpha, T, t)$ is the rate of the reaction (autocatalytic-n^{th} order reaction model)—see Equation (14) [36–38]. The second term in the right-hand side of Equation (12) is the heat generation term (a source term) that is written as a UDF-UDS to incorporate the polymerisation effect (heat of reaction) on the heat transfer.

$$\dot{\alpha}(\alpha, T, t) = (k_1 + k_2 \alpha^m)(1 - \alpha)^n \tag{14}$$

$$k_1 = A_1 \exp\left(\frac{-E_{a_1}}{RT}\right) \tag{15}$$

$$k_2 = A_2 \exp\left(\frac{-E_{a_2}}{RT}\right) \tag{16}$$

where A_1 and A_2 are the pre-exponential constants [1/s], m and n are reaction orders, (E_{a_i}) is the reaction activation energy [J/mol], R is the universal gas constant [J/(mol$\cdot$K)], and T is the temperature [K].

The fluid flow in an LCM process transports species (reactions) that can be defined numerically as a scaler (field variable)—degree of cure. Such a scaler quantity is associated with the relevant phase (liquid) and the other field variables wherewith the linked supplied UDFs (e.g., $\mu(\alpha, T)$) are computed. The degree of cure is calculated using the so-called species transport (Equation (17)) by creating UDFs and a UDS for the convection of the conversion (degree of cure).

$$\phi \frac{\partial \alpha}{\partial t} + (\mathbf{u} \cdot \nabla \alpha) = \phi \dot{\alpha}(\alpha, T, t) \tag{17}$$

The first and second terms at the left-hand side of the above equation are denoted as transient and convection terms, respectively. The rate of reaction ($\dot{\alpha}(\alpha, T, t)$) is added as a source term to link the species transport to the energy equation for the generation of heat. Solving the conservation equations (flow, energy, and species) for the liquid resin moulding of fibrous porous media requires a set of boundary conditions. This includes conditions placed on the inlet, flow-front, and mould-wall (or RUC wall as for the present study) as shown below

$$at\ inlet\ \rightarrow \begin{cases} p = p_0 \\ T = T_0 \\ \alpha = 0 \end{cases} \tag{18}$$

$$at\ flow\ front\ \rightarrow \begin{cases} p = 0 \\ \frac{d(F_r \rho C_p T)}{dt} = \frac{d}{dt} F_r (1 - \phi) \rho_f C_{p_f} \left(T_f - T \right) + F_r \phi \rho_r \Delta H \dot{\alpha}(\alpha, T, t) \\ \frac{d(F_r \alpha)}{dt} = F_r \dot{\alpha}(\alpha, T, t) \end{cases} \tag{19}$$

$$at\ mould\ wall\ \rightarrow \begin{cases} \frac{\partial p}{\partial \mathbf{n}} = 0 \\ T = T_{\mathrm{m}} \end{cases} \tag{20}$$

2.2. Structural Model

2.2.1. Deformation

The in-plane deformation of yarns, at the meso-level, can be explained by a set of geometric equations (see Equation (21) and Figure 2) provided that the yarn width (w), spacing (S), and layer (of fabric) height (h) are known [39]. Here, $\beta(\theta)$—Equation (22)—is the half period of a sinusoid describing the yarn cross-section. Thereby, using a unit cell—the repeating unit cell (RUC) of a plain weave layer—will allow the description of yarn deformation behaviour under injection pressures in addition to the cure reaction time. Accordingly, the total deformation of directional deformations can be then defined.

$$\begin{aligned} \mathrm{Yarn}_1 &= \frac{h}{2}\left[\cos\frac{\pi x}{S} + 1\right] \quad (0 < x < S) \\ \mathrm{Yarn}_2 &= \frac{h}{2}\left[\cos\frac{\pi x}{S} - 1\right] \quad (0 < x < S) \\ \mathrm{Yarn}_3 &= -h\cos\left[\frac{\pi x}{\beta}\right] \quad \left(0 < x < \frac{w}{2}\right) \\ \mathrm{Yarn}_4 &= -h\cos\left[\frac{\pi(x - (S - \beta))}{\beta}\right] \quad \left(S - \frac{w}{2} < x < S\right) \end{aligned} \tag{21}$$

$$\beta(\theta) = \frac{\pi w(\theta)}{2 \arccos\left[\sin^2\left(\frac{\pi w(\theta)}{4S(\theta)}\right)\right]} \tag{22}$$
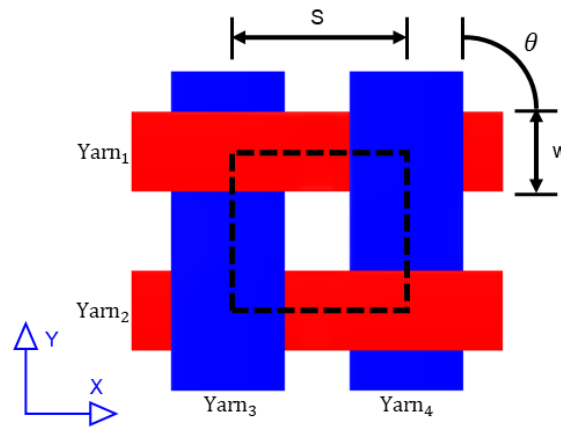
Figure 2. Description for in-plane deformation of yarns subjected to injection pressures or resin curing.

2.2.2. Residual Stress and Strain

Residual stresses (σ_{eq}) and strains (ε_{eq}) can be calculated using the well-known von-Mises method (see Equations (23) and (24)). Such residuals are typically multidirectional and hence can be represented via a scalar (i.e., von-Mises) defined with the stress or strain components for each axis [40–42]. Here, finite element analysis (structural model) is being linked to CFD model so as to import thermal and loading impacts. In doing so, stresses and strains distribution within woven yarns can be analysed, and undesirable effects can be mitigated. von-Mises will also show stresses that remained in the part, mainly, following the mould-filling process (no injection pressures).

$$\sigma_{eq} = \sqrt{\frac{3\left(s_{xx}^2 + s_{yy}^2 + s_{zz}^2\right)}{2} + 3\left(\sigma_{xy}^2 + \sigma_{yz}^2 + \sigma_{zx}^2\right)}$$

With the deviatoric stresses:

$$s_{xx} = +\frac{2}{3}\sigma_{xx} - \frac{1}{3}\sigma_{yy} - \frac{1}{3}\sigma_{zz}$$

$$s_{yy} = -\frac{1}{3}\sigma_{xx} + \frac{2}{3}\sigma_{yy} - \frac{1}{3}\sigma_{zz} \tag{23}$$

$$s_{zz} = -\frac{1}{3}\sigma_{xx} - \frac{1}{3}\sigma_{yy} + \frac{2}{3}\sigma_{zz}$$

$$\varepsilon_{eq} = \frac{2}{3}\sqrt{\frac{3\left(e_{xx}^2 + e_{yy}^2 + e_{zz}^2\right)}{2} + \frac{3\left(\gamma_{xy}^2 + \gamma_{yz}^2 + \gamma_{zx}^2\right)}{4}}$$

With the deviatoric strains:

$$e_{xx} = +\frac{2}{3}\varepsilon_{xx} - \frac{1}{3}\varepsilon_{yy} - \frac{1}{3}\varepsilon_{zz}$$

$$e_{yy} = -\frac{1}{3}\varepsilon_{xx} + \frac{2}{3}\varepsilon_{yy} - \frac{1}{3}\varepsilon_{zz} \tag{24}$$

$$e_{zz} = -\frac{1}{3}\varepsilon_{xx} - \frac{1}{3}\varepsilon_{yy} + \frac{2}{3}\varepsilon_{zz}$$

The engineering strains γ are defined as

$$\gamma_{ij} = 2 \times \varepsilon_{ij} \tag{25}$$

3. Results and Discussion

Tables 1–3 present the required inputs (e.g., cure kinetics parameters) for both models. Simulations are performed at three injection pressures that are presumably low (10 kPa), medium (50 kPa), and high (90 kPa). This will allow us to examine variations in yarn

displacement/deformation during the mould-filling (injection) stage. Since a liquid resin can polymerise (react) unequally when subjected to different temperatures, the present study applies three cure temperatures, in particular 45 °C, 60 °C, and 75 °C— see Figure 3. This means that we can also investigate any incurred stresses or deformations during the cure stage—the conversion of a liquid resin to a thermoset polymer. It is worth noting that the wall temperatures are kept at room temperature ($\sim$25 °C) for all simulations, and then, this increases by 10 °C/min for each cure temperature.

Table 1. Material and process parameters [43].

Description	Parameter	Units
Composite properties	$\rho_r, \rho_f = 1100, 2560$	kg/m^3
	$k_r, k_f = 0.168, 0.0335$	W/(m · K)
	$C_r, C_f = 1680, 670$	J/(kg · K)
Rheology	$\mu_0 = 2.78 \times 10^{-4}$	Pa · s
	$E_\mu = 18,000$	J/mol
	$R = 8.3144$	J/(mol · K)
	$\alpha_{gel} = 0.1$	—
	$a = 1.5$	—
	$b = 1$	—
Cure kinetics	$A_1 = 3.7833 \times 10^5$	s^{-1}
	$A_2 = 6.7833 \times 10^5$	s^{-1}
	$E_{a_1} = 54,418$	J/mol
	$E_{a_2} = 50,232$	J/mol
	$m = 0.3$	—
	$n = 1.7$	—
	$\Delta H = 225 \times 10^3$	J/kg

Table 2. Woven fabric design parameters [44].

Parameter	Value	Parameter	Value
$K_{t_\parallel}$ [m^2]	2.08×10^{-13}	$P_{injection}$ [kPa]	10, 50, 90
$K_{t_\perp}$ [m^2]	2.71×10^{-14}	Width warp yarns [mm]	1.63
V_f[%]	50	Gap warp yarns [mm]	1.16
ϕ_o[%]	50	Width fill yarns [mm]	2.05
ϕ_t[%]	20	Gap fill yarns [mm]	1.09
ϕ_s[%]	37.5		

Table 3. Properties of fibres (carbon fibre) used in the woven model [45].

E_{11} [MPa]	E_{22}, E_{33} [MPa]	v_{12}, v_{13} [−]	v_{23} [−]	G_{12}, G_{13} [MPa]	G_{23} [MPa]
2.9×10^5	2.3×10^4	0.2	0.4	9×10^3	8.214×10^3

Cure profiles with their corresponding cure temperatures are described by Figure 3 for a better illustration. This will show a short period of $\sim$30 s of room temperature during the fill stage, which is followed by an increase of 10 °C/min for the cure stage. This is accomplished by using User-Defined Functions for the wall temperature with an if-statement function so that this wall-temperature is controlled at saturation time with

room temperature ($\sim$25 °C), at post-saturation with heat-up (10 °C/min), then stabilises at (e.g., 60 °C), followed by cool-down (-10 °C/min) until room temperature, and then switched off. From Figure 3, it is obvious that the resin cure conversion is obtained more quickly at 75 °C in contrast to 60 °C and 45 °C. This can be explained by the reaction behaviour of monomers (resin liquid) to heat that stimulates cross-linking (curing) between individual polymer chains and hence, it is higher in heat, quicker in cure. It has to be stressed that heating rates or mould temperatures should always fall within the practical range for a resin type to avoid undesirable outcomes like degradation (burn).
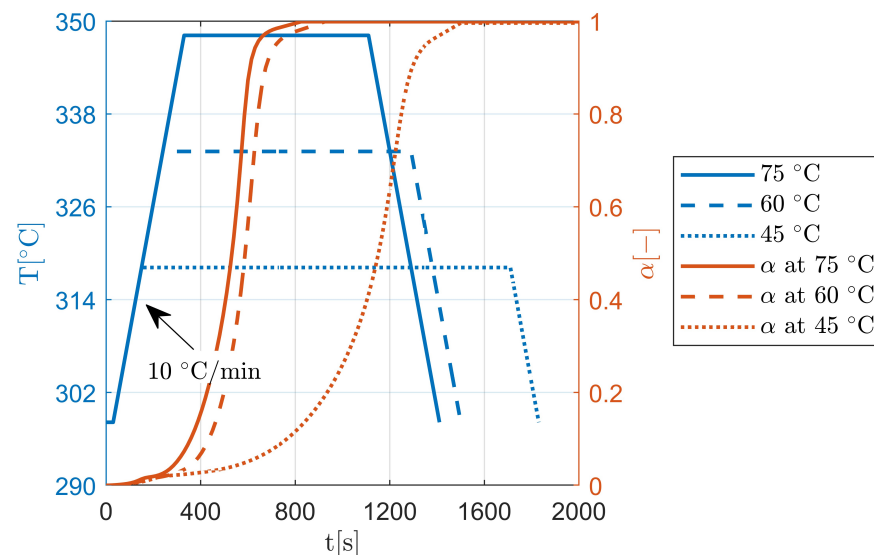
Figure 3. Resin cure profiles at different cure temperatures: 45 °C, 60 °C, and 75 °C.

Figure 4 delivers simulations (visualisation) of the ongoing stresses, strains, and deformations of woven yarns at the meso-level during the saturation time (filling). This shows porous yarns' (structural) interaction with resin (fluid) impregnation (intra- and inter-yarn) in a manner whereby the flow along yarns (e.g., warp yarns) shrinks the bundle slightly, unlike yarns (e.g., weft yarns) that are perpendicular to the flow, which seem to widen as flow infiltrates or penetrates the opposite fibres/filaments, stretching the fibre bundle. Linking the flow (resin) model (finite-volume-based) to the structural (fibrous porous yarns) model (finite-element-based) aids in visualising the distribution of residual stresses within a structure. This is particularly valuable for detecting areas of high stress concentration, which may then be used to influence design adjustments or stress alleviation techniques. Such distribution is heavily influenced by the multi-paradigm modelling framework (within the flow model) that integrates User-Defined Functions together with User-Defined Scalers for micro-permeability, heat transfer, rheology, and cure kinetics, through which the imported pressures or loadings by the structural model are directly affected by the aforementioned multi-physics. Deformations and strains appear to be smaller (approaching zero), and this may be because of the object (yarns and fibres) size (orders of micro-meters)—see Table 4. From Table 4, higher residual stresses are observed at 50 kPa (0.225 MPa) and 90 kPa (0.46 MPa) injection pressures, and this becomes less (5.12×10^{-2}) at lower 10 kPa injection pressure. This manifests a crucial point for real composite manufacturing processes where higher injection pressures (>90 kPa) are used, which may give rise to issues like cracking, warping, or other types of failure at the micro–meso-level.

Table 4. Observations of residual stress–strain and total deformation at maximum during injection time.

Injection Pressure [kPa]	(von-Mises) Stress [MPa]	(von-Mises) Strain $\times 10^{-3}$ [$\mu\varepsilon$]	Total Deformation $\times 10^{-3}$ [μm]
10	5.12×10^{-2}	1.17	0.750
50	0.25575	5.85	3.75
90	0.46035	10.5	6.75
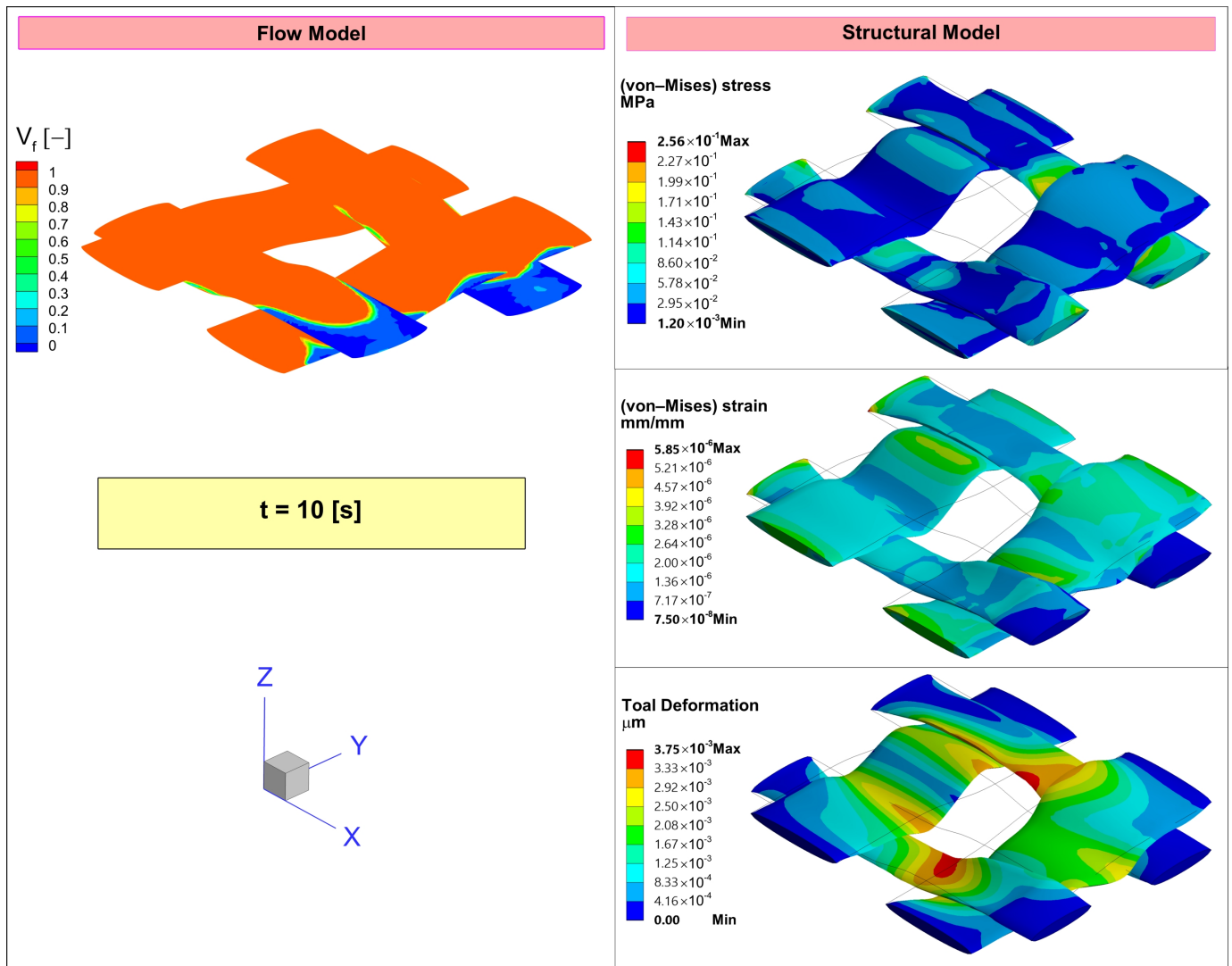
Figure 4. An example of flow–structural linkage simulation at an injection pressure of 50 kPa to demonstrate resin impregnation, yarn residual stress and strain fields (von-Mises), and yarn total deformation, within a representative unit cell (RUC) of a plain weave.

Since the impact of wall temperature (heating) comes after the full resin impregnation of woven fabrics (no more injection), the remaining loads on yarns are the ones left by injection pressures plus the ones provoked by a resin cure reaction (transition from liquid to solid state)—see Figure 5. Thus, weft and warp yarns happen to re-form to their original shape due to no external cause (force), leading to a considerably lower structural response. This indicates that the cure impact is much lower than the injected-flow impact. Table 5 shows the maximum residual stresses, residual strains, and total deformations of woven fabrics (micro–meso-level) at different cure temperatures (45 °C, 60 °C, and 75 °C).

Since the proposed numerical platform is associated with mathematical models and complex 3D geometries, the common challenges for such a paradigm of multi-physics simulations are false diffusion (or error). To address such a phenomenon, a couple of actions can be taken:

1. Use of high-order upwind/interpolation schemes like second-order upwind and third-order MUSCL (Monotone Upstream-Centered Schemes for Conservation Laws)—for FVM analyses.
2. Conversion (or transformation) of highly skewed cells (tetrahedral meshes) to polyhedral—for FVM analyses.
3. Use of under-relaxation factors to control residuals (computed variables) at each iteration—for FVM analyses.
4. Use of pinball radius to prevent penetration during deformation of solids (yarns) (controllable contacts)—for FE analyses.
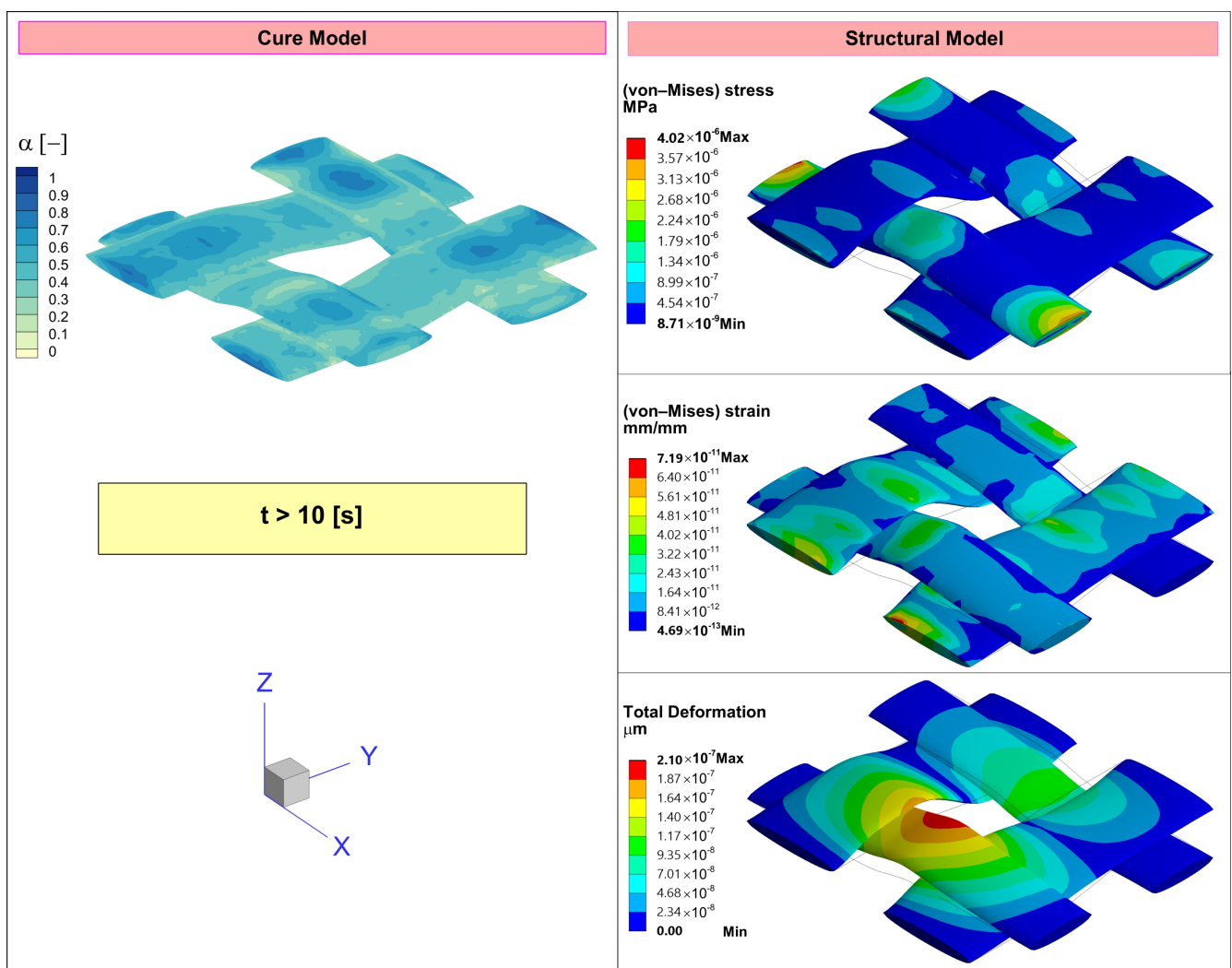
Figure 5. An example of cure-structural linkage simulation at an injection pressure of 50 kPa and a cure temperature of 60 °C to demonstrate resin cure, yarn residual stress and strain fields (von-Mises), and yarn total deformation, within a representative unit cell (RUC) of a plain weave.

Table 5. Observations of residual stress–strain and total deformation at maximum during cure time.

Cure Temperature [°C]	Injection Pressure [kPa]	(von-Mises) Stress $\times 10^{-7}$ [MPa]	(von-Mises) Strain $\times 10^{-9}$ [$\mu\varepsilon$]	Total Deformation $\times 10^{-9}$ [μm]
45	10	1.57	2.69	8.10
	50	40.0	71.7	210
	90	129	236	681
60	10	1.58	2.70	8.15
	50	40.4	72.1	212
	90	130	238	681
75	10	4.89	8.93	25.5
	50	40.8	72.4	213
	90	131	238	688

4. Conclusions

The present paper discusses flow-induced deformation and residual stress–strain in woven fabrics during resin liquid moulding and curing at a meso-level. The study couples a flow/cure model with a structural model for simultaneous data linkage/transfer. This will allow the structural model to import induced loadings during fill and cure stages. The flow/cure model develops UDFs and UDSs to enhance the commercial CFD code by incorporating models like chemo-rheology, cure kinetics, heat generation, and micro-permeability. The study found that higher injection pressures ($\geq$90 kPa), which are normally the case for a real RTM process, can cause higher residual stress–strain, and hence this may give rise to issues like cracking, warping, or other types of failure at the micro–meso-level. Future research work could include chemical shrinkage modelling during the cure process. This may also involve the use of X-ray computed tomography (X-ray CT) and fibre Bragg grating (FBG) sensors to validate and verify the chemical shrinkage percentages (of thermosets).

Author Contributions: Conceptualisation, H.A. and M.J.; Investigation, H.A.; Software, H.A.; Writing—original draft, H.A.; Writing—review and editing, H.A., C.S., D.Z. and M.J.; Supervision; C.S., D.Z. and M.J. All authors have read and agreed to the published version of the manuscript.

Abbreviations

Latin letters:

A_i	Pre-exponential constant [1/s]
C_p	Specific heat [J/kg $\cdot$ K]
E_i	Activation energy [J/mol]
E_{ij}	Young's modulus [MPa]
v_{ij}	Poisson's ratios [$-$]
G_{ij}	Shear modulus [MPa]
f	Model-dependent source term
g	Gravitational acceleration [m/s^2]
H	Reaction heat [J/g]
h	Yarn thickness [mm]

$\mathbf{K}_T$	Thermal conductivity $[\mathrm{W/m \cdot K}]$
$\mathbf{K}_o$	Permeability tensor $[\mathrm{m}^2]$
$\mathbf{K}_t$	Intra-tow permeability $[\mathrm{m}^2]$
p	Pressure $[\mathrm{Pa}]$
$\mathbf{q}$	Heat flux $[\mathrm{W/m}^2]$
R	Universal gas constant $[\mathrm{J/mol \cdot K}]$
S	Length of unit cell base $[\mathrm{mm}]$
T	Temperature $[\mathrm{K}]$
tw	Yarn/Tow width $[\mathrm{mm}]$
t	Time $[\mathrm{s}]$
$\mathbf{u}$	Volume-averaged velocity $[\mathrm{m/s}]$
V_f	Fibre volume fraction $[-]$
$w_{f,r}$	Weight fraction $[-]$

Greek letters:

$\dot{\alpha}$	Rate of reaction $[1/\mathrm{s}]$
α	Degree of cure $[-]$
μ	Dynamic viscosity $[\mathrm{Pa \cdot s}]$
ρ	Density $[\mathrm{kg/m}^3]$
ϕ	Porosity of the medium $[-]$
ψ_i	Nanofiller fraction $[-]$
θ	Angle between warp and weft yarns $[°]$
β	Half period sinusoid of yarn cross-section $[\mathrm{mm}]$
ε_{ij}	Strain $[\mathrm{mm/mm}]$
γ_{ij}	Engineering strain $[\mathrm{mm/mm}]$
σ_{ij}	Stress $[\mathrm{Pa}]$

Subscripts:

$\parallel$	Longitudinal/parallel
$\perp$	Transverse/perpendicular
eq	Equivalent (von)-Mises
f	Fibre/filament
gel	Gelation point
o	Overall/global
r	Resin
s	Inter-tow/mesoscopic
t	Intra-tow/microscopic
x,y,z	Global coordinate system

Superscript:

a, b, m, n	Exponents

References

1. Alotaibi, H.; Abeykoon, C.; Soutis, C.; Jabbari, M. A numerical thermo-chemo-flow analysis of thermoset resin impregnation in lcm processes. *Polymers* **2023**, *15*, 1572. [CrossRef] [PubMed]
2. Meola, C.; Boccardi, S.; Carlomagno, G.M. Chapter 1—Composite materials in the aeronautical industry. In *Infrared Thermography in the Evaluation of Aerospace Composite Materials*; Meola, C., Boccardi, S., Carlomagno, G.M., Eds.; Woodhead Publishing: Cambridge, UK, 2017; pp. 1–24. [CrossRef]
3. Advani, S.G.; Sozer, E.M. 2.23—Liquid molding of thermoset composites. In *Comprehensive Composite Materials*; Kelly, A., Zweben, C., Eds.; Pergamon: Oxford, UK, 2000; pp. 807–844. [CrossRef]
4. Kelly, A.; Zweben, C. Comprehensive composite materials. *Mater. Today* **1999**, *2*, 20–21. [CrossRef]
5. Ermanni, P.; Di Fratta, C.; Trochu, F. Molding: Liquid composite molding(LCM). In *Wiley Encyclopedia of Composites*; John Wiley & Sons, Inc.: Hoboken, NJ, USA, 2012; pp. 1–10. [CrossRef]
6. He, J.H.; He, C.H.; Qian, M.Y.; Alsolami, A.A. Piezoelectric Biosensor based on ultrasensitive MEMS system. *Sens. Actuators Phys.* **2024**, *376*, 115664. [CrossRef]
7. Ma, Y.; Yang, Y.; Sugahara, T.; Hamada, H. A study on the failure behavior and mechanical properties of unidirectional fiber reinforced thermosetting and thermoplastic composites. *Compos. Part B Eng.* **2016**, *99*, 162–172. [CrossRef]
8. Muzzy, J.D.; Kays, A.O. Thermoplastic vs. thermosetting structural composites. *Polym. Compos.* **1984**, *5*, 169–172. [CrossRef]
9. Michaud, V. A review of non-saturated resin flow in liquid composite moulding processes. *Transp. Porous Media* **2016**, *115*, 581–601. [CrossRef]

10. Gonçalves, P.T.; Arteiro, A.; Rocha, N.; Pina, L. Numerical analysis of micro-residual stresses in a carbon/epoxy polymer matrix composite during curing process. *Polymers* **2022**, *14*, 2653. [CrossRef]
11. Yuan, Z.; Wang, Y.; Yang, G.; Tang, A.; Yang, Z.; Li, S.; Li, Y.; Song, D. Evolution of curing residual stresses in composite using multi-scale method. *Compos. Part B Eng.* **2018**, *155*, 49–61. [CrossRef]
12. Dewangan, B.; Chakladar, N. Modelling of residual stress during curing of a polymer under autoclave conditions and experimental validation. *Comput. Mater. Sci.* **2024**, *241*, 113038. [CrossRef]
13. Peng, X.; Xu, J.; Cheng, Y.; Zhang, L.; Yang, J.; Li, Y. An analytical model for cure-induced deformation of composite laminates. *Polymers* **2022**, *14*, 2903. [CrossRef]
14. Kim, D.H.; Kim, S.W.; Lee, I. Evaluation of curing process-induced deformation in plain woven composite structures based on cure kinetics considering various fabric parameters. *Compos. Struct.* **2022**, *287*, 115379. [CrossRef]
15. Fan, S.; Zhang, J.; Wang, B.; Chen, J.; Yang, W.; Liu, W.; Li, Y. A deep learning method for fast predicting curing process-induced deformation of aeronautical composite structures. *Compos. Sci. Technol.* **2023**, *232*, 109844. [CrossRef]
16. Kuentzer, N.; Simacek, P.; Advani, S.G.; Walsh, S. Permeability characterization of dual scale fibrous porous media. *Compos. Part A Appl. Sci. Manuf.* **2006**, *37*, 2057–2068. [CrossRef]
17. Hwang, W.R.; Advani, S.G. Numerical simulations of Stokes–Brinkman equations for permeability prediction of dual scale fibrous porous media. *Phys. Fluids* **2010**, *22*, 113101. [CrossRef]
18. Parnas, R.S.; Salem, A.J.; Sadiq, T.A.; Wang, H.P.; Advani, S.G. The interaction between micro- and macro-scopic flow in RTM preforms. *Compos. Struct.* **1994**, *27*, 93–107. [CrossRef]
19. Parseval, Y.D.; Pillai, K.M.; Advani, S.G. A simple model for the variation of permeability due to partial saturation in dual scale porous media. *Transp. Porous Media* **1997**, *27*, 243–264. [CrossRef]
20. Gascón, L.; García, J.A.; LeBel, F.; Ruiz, E.; Trochu, F. A two-phase flow model to simulate mold filling and saturation in Resin Transfer Molding. *Int. J. Mater. Form.* **2016**, *9*, 229–239. [CrossRef]
21. Happel, J. Viscous flow relative to arrays of cylinders. *AIChE J.* **1959**, *5*, 174–177. [CrossRef]
22. Sangani, A.S.; Acrivos, A. Slow flow past periodic arrays of cylinders with application to heat transfer. *Int. J. Multiph. Flow* **1982**, *8*, 193–206. [CrossRef]
23. Drummond, J.E.; Tahir, M.I. Laminar viscous flow through regular arrays of parallel solid cylinders. *Int. J. Multiph. Flow* **1984**, *10*, 515–540. [CrossRef]
24. Gutowski, T.G.; Cai, Z.; Bauer, S.; Boucher, D.; Kingery, J.; Wineman, S. Consolidation experiments for laminate composites. *J. Compos. Mater.* **1987**, *21*, 650–669. [CrossRef]
25. Gebart, B.R. Permeability of unidirectional reinforcements for RTM. *J. Compos. Mater.* **1992**, *26*, 1100–1133. [CrossRef]
26. Cai, Z.; Berdichevsky, A.L. An improved self-consistent method for estimating the permeability of a fiber assembly. *Polym. Compos.* **1993**, *14*, 314–323. [CrossRef]
27. Phelan, F.R.; Wise, G. Analysis of transverse flow in aligned fibrous porous media. *Compos. Part A Appl. Sci. Manuf.* **1996**, *27*, 25–34. [CrossRef]
28. Woerdeman, D.L.; Phelan, F.R.; Parnas, R.S. Interpretation of 3-D permeability measurements for RTM modeling. *Polym. Compos.* **1995**, *16*, 470–480. [CrossRef]
29. Castro, J.M.; Macosko, C.W. Studies of mold filling and curing in the reaction injection molding process. *AIChE J.* **1982**, *28*, 250–260. [CrossRef]
30. Bruschke, M.V.; Advani, S.G. A numerical approach to model non-isothermal viscous flow through fibrous media with free surfaces. *Int. J. Numer. Methods Fluids* **1994**, *19*, 575–603. [CrossRef]
31. Abbassi, A.; Shahnazari, M.R. Numerical modeling of mold filling and curing in non-isothermal RTM process. *Appl. Therm. Eng.* **2004**, *24*, 2453–2465. [CrossRef]
32. Shojaei, A.; Ghaffarian, S.R.; Karimian, S.M.H. Modeling and simulation approaches in the resin transfer molding process: A review. *Polym. Compos.* **2003**, *24*, 525–544. [CrossRef]
33. Antonucci, V.; Giordano, M.; Nicolais, L.; Di Vita, G. A simulation of the non-isothermal resin transfer molding process. *Polym. Eng. Sci.* **2000**, *40*, 2471–2481. [CrossRef]
34. Liu, B.; Advani, S.G. Operator splitting scheme for 3-D temperature solution based on 2-D flow approximation. *Comput. Mech.* **1995**, *16*, 74–82. [CrossRef]
35. Dessenberger, R.B.; Tucker, C.L. Thermal dispersion in resin transfer molding. *Polym. Compos.* **1995**, *16*, 495–506. [CrossRef]
36. Kamal, M.R.; Sourour, S. Kinetics and thermal characterization of thermoset cure. *Polym. Eng. Sci.* **1973**, *13*, 59–64. [CrossRef]
37. Sourour, S.; Kamal, M.R. Differential scanning calorimetry of epoxy cure: Isothermal cure kinetics. *Thermochim. Acta* **1976**, *14*, 41–59. [CrossRef]
38. Kamal, M.R. Thermoset characterization for moldability analysis. *Polym. Eng. Sci.* **1974**, *14*, 231–239. [CrossRef]
39. McBride, T.; Chen, J. Unit-cell geometry in plain-weave fabrics during shear deformations. *Compos. Sci. Technol.* **1997**, *57*, 345–351. [CrossRef]
40. Wang, Q.; Yang, X.; Zhao, H.; Zhang, X.; Cao, G.; Ren, M. Microscopic residual stresses analysis and multi-objective optimization for 3D woven composites. *Compos. Part A Appl. Sci. Manuf.* **2021**, *144*, 106310. [CrossRef]
41. Li, H.; Bacarreza, O.; Khodaei, Z.S.; Ferri Aliabadi, M.H. Probabilistic multi-scale design of 2D plain woven composites considering meso-scale uncertainties. *Compos. Struct.* **2022**, *300*, 116099. [CrossRef]

42. Yang, N.; Zou, Z.; Potluri, P.; Soutis, C.; Katnam, K.B. Intra-yarn fibre hybridisation effect on homogenised elastic properties and micro and meso-stress analysis of 2D woven laminae: Two-scale FE model. *Compos. Struct.* **2024**, *344*, 118358. [CrossRef]
43. Shojaei, A.; Ghaffarian, S.R.; Karimian, S.M. Three-dimensional process cycle simulation of composite parts manufactured by resin transfer molding. *Compos. Struct.* **2004**, *65*, 381–390. [CrossRef]
44. Alotaibi, H.; Jabbari, M.; Abeykoon, C.; Soutis, C. Numerical investigation of multi-scale characteristics of single and multi-layered woven structures. *Appl. Compos. Mater.* **2022**, *29*, 405–421. [CrossRef]
45. ANSYS Mechanical Enterprise. *Engineering Data (Software ANSYS)*, Version 19.2; ANSYS, Inc.: Canonsburg, PA, USA, 2018.